Hierarchical Core-Shell Co_2N/CoP Embedded in N, P-doped Carbon Nanotubes as Efficient Oxygen Reduction Reaction Catalysts for Zn-air Batteries

Chongchao Yao, Jiaxin Li, Zhihao Zhang, Chunli Gou, Zhongshen Zhang, Gang Pan, Jing Zhang*

C. C. Yao, J. X. Li, C. L. Gou, Prof. Z. S. Zhang and Prof. J. Zhang

National Engineering Laboratory for VOCs Pollution Control Material & Technology, Research Center for Environmental Material and Pollution Control Technology, University of Chinese Academy of Sciences, Beijing, 101408, P.R. China

Research Center for Environmental Material and Pollution Control Technology, University of Chinese Academy of Sciences, Beijing, 101408, P.R. China.

E-mail: jingzhang@ucas.ac.cn

Prof. G. Pan

Integrated Water-Energy-Food Facility (iWEF), school of Animal, Rural and Environmental Sciences, Nottingham Trent University, Nottinghamshire NG25 0QF, United Kingdom.

Z. H. Zhang

Key laboratory of Environmental Nanotechnology and Health Effects, Research Center for Eco-Environmental Sciences, Beijing, 100085, P.R. China.

Key words

Core-shell electrocatalysts, N, P doping, synergistic effects, oxygen reduction reaction, Zn-air batteries

Abstract

Projecting a cost-effective and highly efficient electrocatalyst for oxygen reaction reduction (ORR) counts a great deal for Zn-air batteries. Herein, we have developed a hierarchical core-shell ORR catalyst (Co_2N/CoP@PNCNTs) by embedding cobalt phosphides and/or cobalt nitrides as the core into N, P-doped carbon nanotubes (PNCNTs) as the shell via one-step carbonization, nitridation and phosphorization of pyrolyzing Co-MOF precursor. The globally N, P-doped structure of Co_2N/CoP@PNCNTs demonstrates an outstanding electrocatalytic activity in the alkaline solution with the onset and half-wave potentials of 1.07 V and 0.85 V respectively. Moreover, a Zn-air battery assembled from Co_2N/CoP@PNCNTs as the air cathode delivers an open circuit potential of 1.49 V, a maximum power density of 151.1 mW cm^{-2} and a specific capacity of 823.8 mAh kg^{-1}. It is reflected that Co_2N/CoP@PNCNTs provides a long-term durability with a slight decline of 15 h in the chronoamperometry measurement and an excellent charge-discharge stability with negligible voltage decay for 150 h at 10 mA cm^{-2} in Zn-air batteries. The results reveal that Co_2N/CoP@PNCNTs has superiority over most Co-N_x-C or Co_xP@C catalysts reported so far. The excellent catalytic properties and stability of Co_2N/CoP@PNCNTs derive from synergistic effects between Co_2N/CoP and mesoporous N, P-doped carbon nanotubes.

Introduction

Many forms of apinoid, renewable, highly efficient energy conversion and storge systems such as proton exchange membrane fuel cells (PEMFCs),[1] metal-air batteries[2-4] and overall water splitting[5, 6] have aroused intensive and accelerated attentions because of depletion of irreplaceable fossil fuels and severe worldwide environmental pollution.[7-9] Zn-air batteries have been recognized as one of the most potential metal-air batteries owing to high energy density.[10] In Zn-air batteries, the half-reactions such as oxygen reduction reaction (ORR) play a crucial role in achieving high energy densities.[11, 12] Pt-based noble metal catalysts are often selected to get a high performance of electrochemical properties. However, the prohibitive cost originated from scarcity and unsatisfying stability of Pt-based catalysts block the scale-up implementation of the above energy devices.[8, 13, 14] Therefore, it is urgently demanded to exploit alternatively non-noble metal catalysts comprised of earth-abundant, cost-effective and durable properties.

In recent years, earth-abundant cobalt catalysts including hydroxides, oxides, sulfides, nitrides and phosphides have attracted increasing research interest due to their inexpensive cost and qualified electrocatalytic activities for ORR,[13, 15-17] oxygen evolution reaction (OER)[18-20] and hydrogen evolution reaction (HER).[16, 20, 21] To date, various cobalt electrolytes coupled with nitrogen-doped carbon materials (Co-N_x-C) have been widely reported due to their excellent conductivity and electrochemical activity for ORR and OER.[13, 18, 22-24] For example, Yuan et al. performed Fe/Co-N_x-C, using silica-protected Fe/Co-polyporphyrin synthetic

strategies to achieve both a good electrocatalytic activity with a half-wave potential of 0.86 V vs RHE in alkaline media and a high peak power density of 152 mW cm^{-2} in assembled Zn-air batteries.[25] However, Co-N_x-C moieties have been reported to degrade quickly under harsh alkaline conditions, leading to poor stability for ORR and OER.[25] In addition, the transition metal phosphides have drawn considerable concerns, owing to their promising activity and stability for HER and OER,[27-30] nevertheless lacking of necessary active sites for ORR process.[31] For example, Yang et.al fabricated urchin-like CoP nanocrystals with an exceptional low overpotential of 180 mV for HER, yet an unsatisfactory half-potential of 0.7 V for ORR.[16] Additionally, the cobalt phosphides (Co_xP) reported for ORR/OER/HER effective catalysis mainly contain Co_2P and CoP.[27, 33-35] Shi et al. successfully developed Co_xP@NPC ($0<x<2$, Co_2P, Co_2P/CoP, CoP) for bifunctional OER/ORR electrocatalysts and found Co_2P@NPC possessed the superior ORR/OER activity and a peak power density of 157 mW cm^{-2} for as-constructed Zn-air batteries.[36] Liu et al. discovered that among all the Co_xP phases, Co_2P had the optimal electrocatalytic preferences for ORR/OER/HER with the density functional theory calculations.[35] Despite all the advances, the phases tendency of cobalt phosphides for ORR is not clear yet. Therefore, more research efforts are demanded for addressing the synergistic effects and exploring the controllable fabrication of cobalt phosphides with varied phases for ORR.[34]

Although there are many reports on Co_2N, CoP and heteroatoms doped carbon for electrocatalytic applications, these reported catalysts still show many deficiencies in

the electrocatalytic activity or stability in the ORR testing. Herein, we propose an "icing on the cake" strategy by combining the Co_2N or Co_2N/CoP as the core with N, P-doped carbon nanotubes as the shell to realize excellent electrocatalytic activities for ORR. The as-constructed Co@C, CoP@PC, Co_2N@NCNTs and Co_2N/CoP@PNCNTs were obtained through pyrolyzing Co-MOF precursor with dicyandiamide as the N-doping source as well as NaH_2PO_2 as the P-doping source. Interestingly, CoP only existed in the condition of mass ratio of 1:10 (the precursor and NaH_2PO_2) at 800 °C in CoP@PC and Co_2N/CoP@PNCNTs. Co_2P appeared under other circumstances. Among all the synthesized samples, the Co_2N/CoP@PNCNTs behaves the best electrocatalytic activity and stability for ORR and Zn-air batteries. Co_2N/CoP@PNCNTs is not only employed as an ORR electrocatalyst with the onset and half-wave potentials of 1.07 V and 0.85 V separately but also as an outstanding air cathode catalyst for Zn-air batteries reaching a peak power density of 151.1 mW cm^{-2} and a specific capacity of 823.8 mAh kg^{-1}. The superior performances exhibit uncontemplated phenomena that CoP possesses a better potentiality than Co_2P and multicomponent Co_2N/CoP or Co_2N/Co_2P overmatches monocomponent Co_2N or CoP toward ORR. This work provides a novel strategy by combining multicomponent cobalt phosphides with heteroatom-doped carbon nanotubes for high-performance ORR electrocatalysis in sustainable energy conversion systems.

2. Results and Discussion

The synthetic approaches of Co-MOF, Co_2N@NCNTs, Co_2N/CoP@PNCNTs using

$Co(Ac)_2.4H_2O$, 2-aminoterephthalic acid, dicyandiamide and NaH_2PO_2 as raw materials were depicted in **Scheme 1**. The synthesis began with $Co(Ac)_2.4H_2O$ and 2-aminoterephthalic acid to form a uniform Co-MOF precursor. Then, the Co-MOF precursor was carbonized and azotized with DCDA as carbon and nitrogen source via the temperature-programmed process to produce Co_2N@NCNTs. It led to isolated Co coordinated with N nanoparticles embedded into N-doped carbon-nanotube matrix. Co_2N/CoP@PNCNTs was obtained by pyrolyzing the same precursor and the similar procedure of one-step carbonization, nitridation and phosphorization.

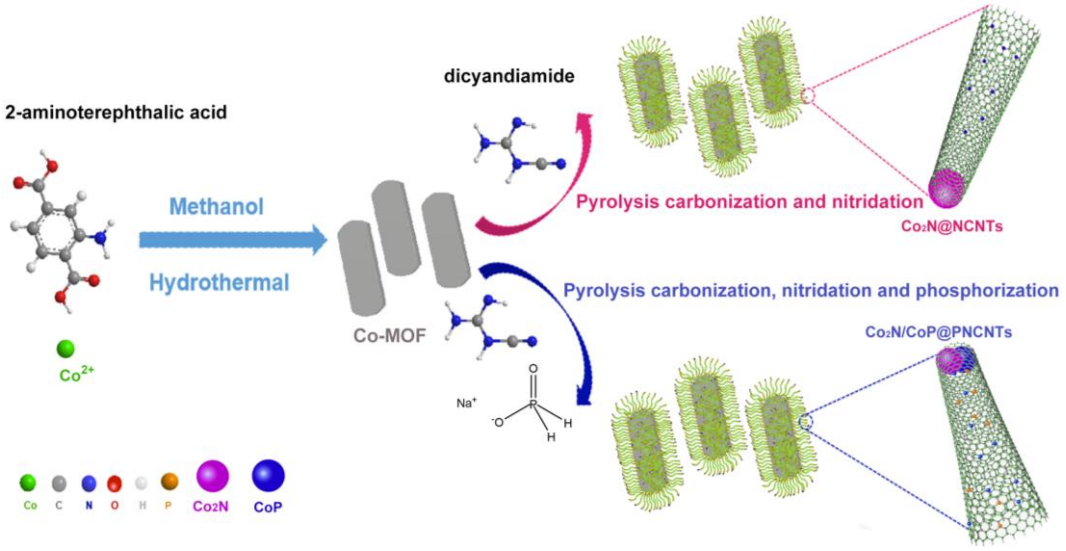

Scheme1 Schematic illustration for the preparation strategy of Co_2N@NCNTs and Co_2N/CoP@PN-CNTs.

Figure 1 and **Figure S1** present the environmental scanning electron microscope (ESEM) images of the obtained Co-MOF precursor as well as the products named Co_2N@NCNTs and Co_2N/CoP@PNCNTs. Co-MOF presents the smooth surface and uniform 4-5 μm microrods (**Figure S1a**, Supporting Information). However, the products of Co_2N@NCNTs and Co_2N/CoP@PNCNTs obtained from pyrolysis are

covered with 20-25 μm uniform nanotubes in diameter on the microrods (**Figure 1a**, **1e**). DCDA as both carbon and nitrogen sources and NaH_2PO_2 as phosphorus source lead to the growth of carbon nanotubes[36] and formation of cobalt phosphides, respectively[38] during the carbonization, nitridation and phosphorization. Remarkably, the carbonization temperature is proved to be a critical factor to regulate the morphology and structure of Co_2N@NCNTs and Co_2N/CoP@PNCNTs. With the increasing temperature from 700 °C, 800 °C to 900 °C, the carbon substrate appears only partial nanotubes mainly ascribed to the incomplete pyrolysis,[39] fully covered with nanotubes and bigger nanoparticles which gradually collapsed respectively in **Figure S1b-e** (Supporting Information). In addition, the EDS elemental mappings of Co_2N@NCNTs and Co_2N/CoP@PNCNTs show that C, O, N, Co, P elements are homogeneously distributed on the materials (**Figure S2-S3**, Supporting Information). Furthermore, the morphology and elemental compositions of Co@C and CoP@PC are demonstrated from ESEM and corresponding mapping EDS element images. ESEM and corresponding mapping EDS element images in **Figure S4 and Figure S5** (Supporting Information) indicate that for both Co@C and CoP@PC, the obtained carbon substrates are covered with uniform nanoparticles of 50-200 nm, where C, O, Co and P elements are homogeneously distributed on their surfaces.

As presented in **Figure 1**, transmission electron microscopy (TEM) images of Co_2N@NCNTs and Co_2N/CoP@PNCNTs reveal that the nanoparticles with a diameter of about 10 nm are embedded within carbon nanotubes to form the core-shell structures (**Figure 1b**, **1e**). The Co_2N@NCNTs and Co_2N/CoP@PNCNTs were

further characterized by high-resolution transmission electron microscopy (HR-TEM). As shown in **Figure 1c** and **1f**, the graphite-like layers with an interlayer spacing of 0.354 nm related to the (002) lattice fringes of graphitic carbon[40] can be identified, which can originate from the amorphous carbon during the high-temperature process. Moreover, the Co_2N crystal structure displays high-ordered lattice fringes spaced by 0.209 nm, corresponding to its (021) plane.[41-42] Furthermore, a lattice spacing of 0.245 nm can be observed from the Co_2N/CoP@PNCNTs, which is analogous to the (102) plane of CoP.[43-45] Meanwhile, TEM and HR-TEM images of CoP@PC in **Figure S6** (Supporting Information) manifest that nanoparticles are embedded in the graphitic-like layer and the CoP crystal structure displays high-ordered lattice fringes with the spacings of 0.243 nm, in accordance with its (102) plane.

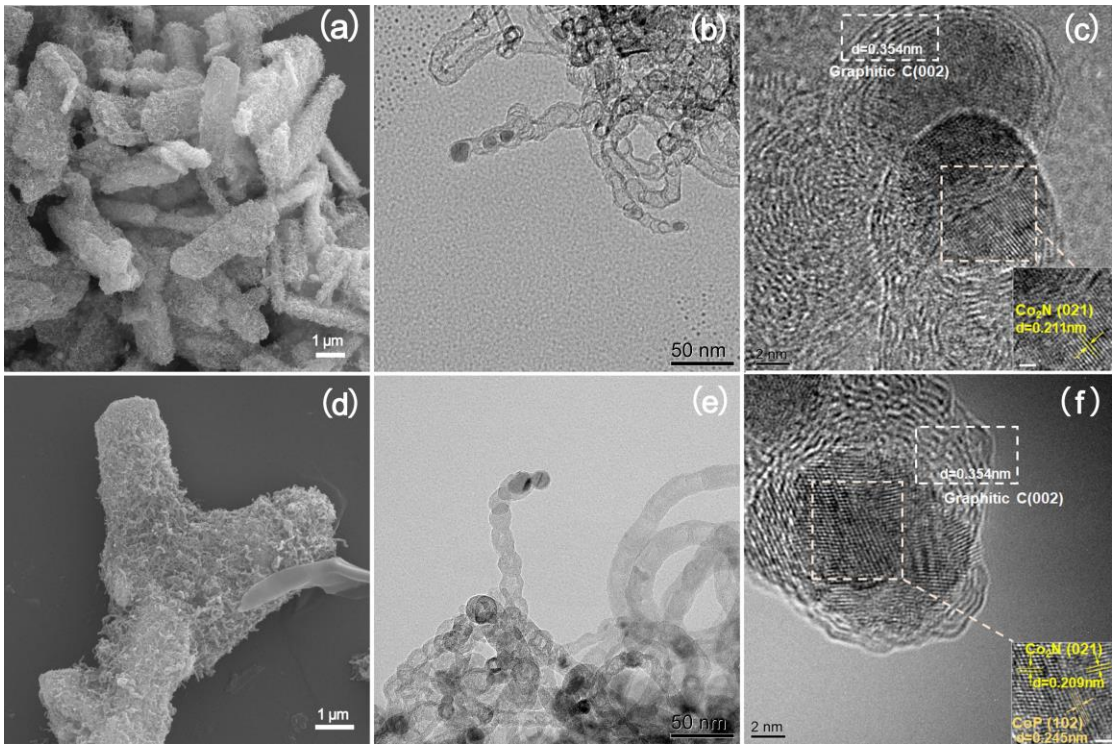

Figure 1. Morphology and structure of Co_2N@NCNTs and Co_2N/CoP@PNCNTs. a, d) ESEM images of Co_2N@NCNTs and Co_2N/CoP@PNCNTs; b, c) TEM images and HR-TEM

images of Co_2N@NCNTs; e, f) TEM images and HR-TEM images of Co_2N/CoP@PNCNTs. Yellow and orange arrows indicate the lattice fringes of cobalt nitride, cobalt phosphide.

The crystal texture of as prepared Co_2N@NCNTs and Co_2N/CoP@PNCNTs by X-ray diffraction (XRD) patterns and analyses are shown in **Figure 2a** and **Figure S7** (Supporting Information). Both Co_2N@NCNTs and Co_2N/CoP@PNCNTs (**Figure 2a**) have an obvious diffraction peak at $2\theta = 44.5°$ matched with the (021) plane of Co_2N (JCPDS No. 72-1368).[46, 47] Furthermore, the peak at 26.2° indicates the formation of graphite carbon corresponding to the C (002) plane (JCPDS No. 01-1061).[40, 48] Compared with Co_2N/CoP@PNCNTs, Co_2N@NCNTs exposes peaks at 51.5° and 78.9° corresponding to metallic Co (JCPDS No. 89-7093),[48, 49] whereas a different peak at 36.7° assigned to the (102) plane of CoP (JCPDS No. 029-0497) [50] is observed in Co_2N/CoP@PNCNTs, which implies that Co was transformed into CoP during the phosphorization. The phases obtained at different temperatures and mass ratios of Co-MOF/NaH_2PO_2 are summarized in **Table S1** (Supporting Information). Consequently, CoP is generated only in the Co_2N/CoP@PNCNTs with pyrolysis temperature at 800 °C and mass ratio of the precursor and NaH_2PO_2 of 1:10. Co_2P exists in other temperatures and mass ratios of Co_2N/Co_2P@PNCNTs. In addition, the successful generation of Co@C and CoP@PC was also confirmed by X-ray diffraction (XRD) patterns in **Figure S12a** (Supporting Information). Co@C displays diffraction peaks identical to the graphitic C (JCPDS No. 01-1061) and Co^0 (JCPDS No. 89-7093). For CoP@PC, the similar outcome occurs in the diffraction peaks of at 36.7° and 56.8° in accordance with the (102) and (301) planes of CoP (JCPDS No.

29-0497), indicating the successful formation of CoP.

The specific surface areas and porosity of the prepared Co_2N@NCNTs and Co_2N/CoP@PNCNTs were performed by N_2 physisorption measurements. The N_2 adsorption/desorption and pore distributions isotherms of Co_2N@NCNTs and Co_2N/CoP@PNCNTs show a type-IV behavior in **Figure 2b**. The Co_2N/CoP@PN-CNTs presents a larger specific surface area (148.4 $m^2 g^{-1}$) than the Co_2N@NCNTs (101.1 $m^2 g^{-1}$), which signifies heteroatom P doping has improved the reaction surface area. Moreover, the pore size distributions of catalysts exhibit dominant mesoporous structures which are mainly centered at around 4.0 nm in Co_2N@NCNTs and Co_2N/CoP@PNCNTs. As shown in **Figure S12b-c** (Supporting Information), the N_2 adsorption/desorption and pore distributions isotherms of CoP@PC exhibit a mesoporous structure with a specific surface area of 84.4 $m^2 g^{-1}$. However, Co@C has a less porous structure and a lower specific surface area (33.4 $m^2 g^{-1}$), as compared to CoP@PC. The specific surfaces and porosity of these samples are listed in **Figure S8a-b and Figure S12c** (Supporting Information). The above results reveal that the Co_2N/CoP@PNCNTs possesses the largest specific surface area which is critical for making a good contact between free gas and electrolyte and exposing more active sites.

The Raman spectra of Co_2N@NCNTs and Co_2N/CoP@PNCNTs (**Figure 2c**) exhibit two broad peaks which are designated as D band (1350 cm^{-1}) and G band (1588 cm^{-1}), reflecting the A_{1g} vibration mode of disorder sp^3 carbon atoms and the E_{2g} vibration mode of sp^2-hybridized carbon atoms, respectively.[51, 52] The intensity

ratio of these two peaks (I_D/I_G) in the spectrum of Co_2N/CoP@PNCNTs is 0.96 and this value is lower than that of Co_2N@NCNTs (1.04). The result shows that the presence of highly graphitized CNTs in Co_2N/CoP@PNCNTs is beneficial to the fast electron transfer in the following electrochemical reactions. The other samples of Co_2N@NCNTs and Co_2N/Co_xP@PNCNTs with different temperatures and ratios are calculated and presented in **Figure S9** and **S10** (Supporting Information), demonstrating Co_2N/CoP-@PNCNTs possesses the lowest value of I_D/I_G and the superior graphitized degree. The FT-IR spectra of Co_2N@NCNTs and Co_2N/CoP@PNCNTs in **Figure 2d** show the typic peaks at 1154 cm^{-1} and 1550 cm^{-1} respectively belonging to C-POOH and C-N,[53, 54] indicating P and N doped in the carbon nanotubes. In addition, the Raman spectra of Co@C and CoP@PC in **Figure S12d** (Supporting Information) further verify that Co@C has a lower I_D/I_G value, indicating a higher degree of graphitic carbon. The special groups of Co@C and CoP@PC were investigated by FT-IR spectra measurements. **Figure S12e** (Supporting Information) shows the typic peaks at 1554 cm^{-1} belonging to C-POOH, [53] suggesting that P is doped in the CoP@PC.

The elemental composition and chemical state of the catalysts were probed by X-ray photoelectron spectroscopy (XPS). C, N, O, P and Co were detected in Co_2N/CoP-@PNCNTs from the wide survey spectra in **Figure S11a** (Supporting Information). The high-resolution P 2p spectrum can be deconvoluted into four bonding types, which indicates P doped into the carbon support in agreement with the FT-IR results (the inset of **Figure S11a**, Supporting Information). The high-resolution N 1s spectra

of both Co_2N@NCNTs and Co_2N/CoP@PNCNTs (**Figure S11b**, Supporting Information) display four main peaks: pyridinic-N (398.8 eV), Co-N_x (399.4 eV), pyrrolic-N (400.3 eV) and graphitic-N (401.3 eV).[18, 36, 53, 55-58] In contrast with other N species,[18] pyridinic N dopant sites are generally accepted as effective catalytic sites for ORR, owing to reducing the energy barrier for adsorption of O_2 on adjacent carbon atoms.[18, 59, 60] Compared with Co_2N@NCNTs, the content of pyridinic-N in Co_2N/CoP@PN-CNTs increases from 35.5% to 45.7%, which is favorable for better catalytic efficiency for ORR (**Table S2**, Supporting Information). In **Figure 2e**, two fitted peaks of the Co 2p region are located at 780.1 eV and 796.0 eV, which are consistent with Co $2p_{3/2}$ and Co $2p_{1/2}$ respectively.[18] The $Co2p_{3/2}$ and $Co2p_{1/2}$ further spilt into subpeaks of Co (III) and Co (II) (**Table S3,** Supporting Information). The observation of subpeaks for both materials at 780.1 eV confirms that Co (III) may combine with N-dopants to form Co-N_x species which can generate effective electrocatalytically active sites for ORR.[13, 58, 61, 62] Compared with the peak in accordance with Co-O (781.6 eV) in Co_2N@NCNTs, the peak corresponding to Co-P (781.5 eV)[55, 63] in Co_2N/CoP@PNCNTs indicates that O coordinating with Co was substituted by P (**Figure 2f** and **Table S3**, Supporting Information). Additionally, compared with Co_2N@NCNTs, the content of N and O decreases and the content of P increases in Co_2N/CoP@PNCNTs, again confirming that partial N and O are substituted by P (**Table S4,** Supporting Information). Furthermore, the positive shift of Co $2p_{3/2}$ (780.3 eV) and the negative shift of P $2p_{3/2}$ (129.6 eV) compared with metallic Co (777.9 eV) and elemental P (130.2 eV) manifest the electron transfer from

Co to P.[63] In addition, two satellite peaks at 786.1 eV and 803.1 eV can be related to the excitation of high-spin Co(II).[7, 62, 64] Further deconvoluted high-resolution C 1s in **Figure 2f** validates the Co_2N@NCNTs with bands of carbon in graphite (C=C/C-C) at 284.5 eV,[55] carbon singly bound to nitrogen (C-N, 44.1 wt%) at 285.0 eV,[54] carbon singly bound to hydrogen-oxygen bond (C-OH) at 286.3 eV, carbon bound to two oxygens (O=C-O) at 288.8 eV.[67] The C-N at 285.0 eV and C-P at 286.0 eV[55, 56, 68] in the Co_2N/CoP@PNCNTs indicate the incorporation of N and P into the C skeleton in accordance with the P 2p and FT-IR results.

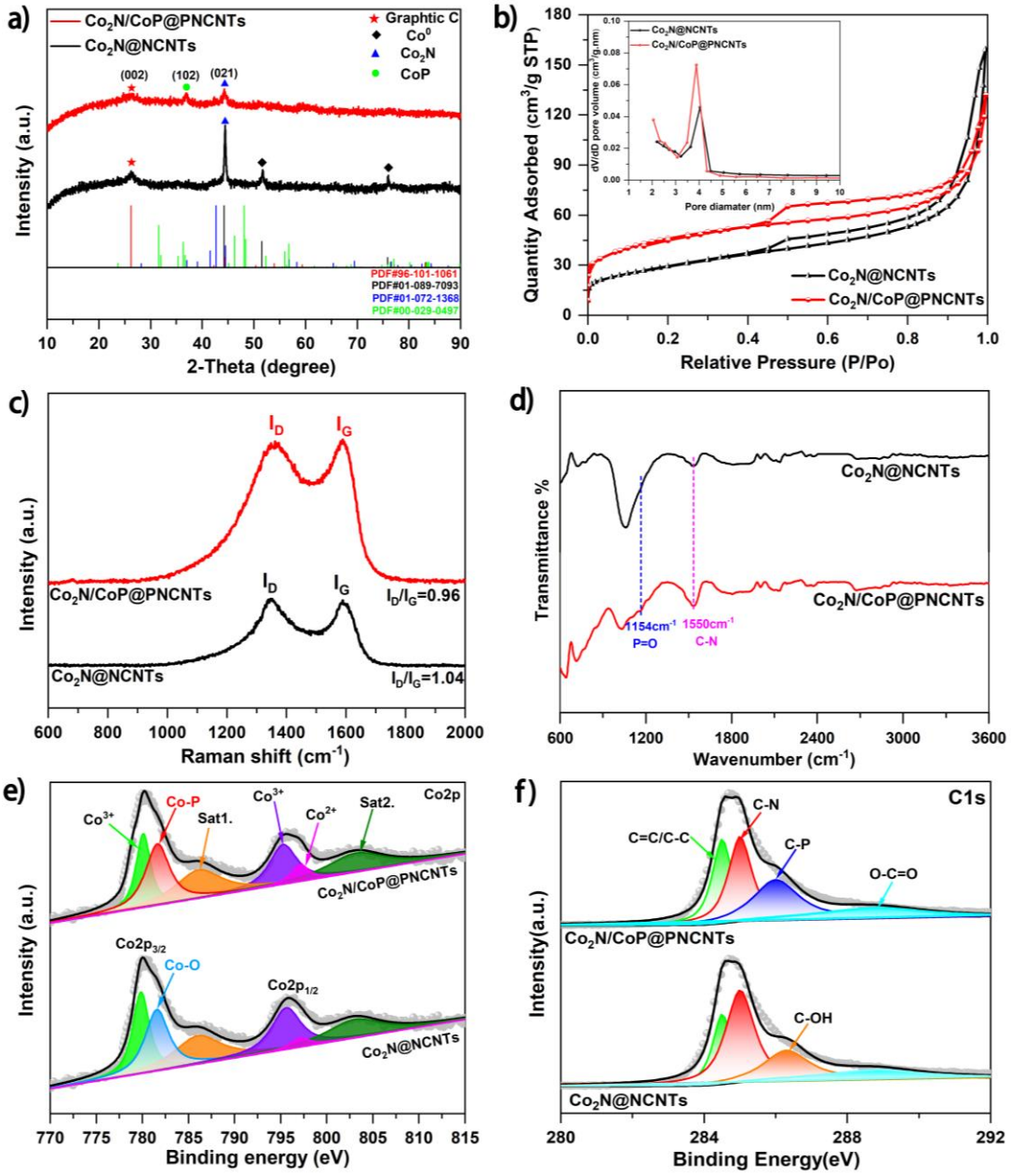

Figure 2. a) XRD patterns of Co_2N@NCNTs and Co_2N/CoP@PNCNTs; b) N_2 adsorption/desorption isotherms of Co_2N@NCNTs and Co_2N/CoP@PNCNTs, with the corresponding pore size distribution shown in the inset; c, d) Raman and FT-IR spectra of Co_2N@NCNTs and Co_2N/CoP@PNCNTs; High-resolution XPS spectra of Co_2N@NCNTs and Co_2N/CoP@PNCNTs: e) Co 2p; f) N1s.

The catalytic activities of the Co_2N@NCNTs and Co_2N/CoP@PNCNTs catalysts toward ORR were recorded in an O_2-saturated 0.1 M KOH solution by cyclic

voltammetry (CV) in **Figure 3a-b and Figure S13** (Supporting Information). The Co_2N@NCNTs and Co_2N/CoP@PNCNTs reveal a superior performance in the CV scanning among all of the Co_2N@NCNTs and Co_2N/Co_xP@PNCNTs catalysts (**Figure S13a**, **c**, **d**, Supporting Information). The Co_2N/CoP@PNCNTs shows more positive peak potential at about 0.85 V than Co_2N@NCNTs (0.84 V) and Pt/C (0.83 V). As shown in **Figure 3b**, the CV curve of the Co_2N/CoP@PNCNTs in O_2-saturated solution appears an obvious reduction peak with a favorable response for ORR, while featureless peaks in N_2-saturated solution. A similar result appears in the Co_2N@NCNTs in **Figure S13b** (Supporting Information), suggesting apparent ORR response performances. The electrocatalytic activities of these catalysts **(Figure 3c-e** and **Figure S14-S16**, Supporting Information) were further investigated based on RDE and RRDE measurements in 0.1 M KOH solution. The related parameters of ORR performance on the different catalysts are compared in **Figure S14d** (Supporting Information). As presented in **Figure 3c** and **Figure S14d**, the Co_2N/CoP@PNCNTs presents the best ORR activity with an onset potential E_{onset} (1.07 V vs. RHE) and a half-wave potential $E_{1/2}$ (0.85 V vs. RHE), both of which are more positive than Pt/C (E_{onset} 0.95 V, $E_{1/2}$ 0.82 V) as well as Co_2N@NCNTs (E_{onset} 1.00 V, $E_{1/2}$ 0.83 V). The half-wave potential distinguishes a 30 mV between Co_2N/CoP@PNCNTs and Pt/C. The Koutecky-Levich (K-L) plots of Co_2N/CoP@PNCNTs were used to assess the kinetic activity in **Figure 3d**. Consequently, the K-L plots exhibit a good linearity between the current density and the increasing rotation speeds, indicating the first order reaction kinetics in connection with the concentration of dissolved O_2 at the

various potentials.[69] From the slopes of K-L plots in the potential range of 0.25 V-0.6 V, the average electron transfer number is 3.94, equivalent to the theoretical value 4.0. It implies the Co_2N/CoP@PNCNTs dominates oxygen reduction via the four-electron pathway. Based on RRDE results corresponding to the ring and disk current density (**Figure S16d**, Supporting Information), the transfer electron number can be further confirmed as 3.95-3.99 which is approximately close to 4 as presented in **Figure 3e**. In addition, the H_2O_2 yield is calculated to be 2.5 % at the range of 0.2 V to 0.8 V, suggesting an outstanding selectivity of $4e^-$ ORR pathway. Meanwhile, the Tafel slope of Co_2N/CoP@PNCNTs is as small as 89 mV dec^{-1}, remarkably lower than that of Pt/C (116 mV dec^{-1}) in **Figure 3f**, demonstrating faster reaction kinetics.[18, 28, 69-71] The admirable methanol resistance and durability of Co_2N/CoP@PNCNTs can be stated incontestably by the chronoamperometric response in **Figure 3g-h**. It only shows a slight cathodic current attenuation of 4.7 % in 15 h compared to the Co_2N@NCNTs (10.1 %) and Pt/C (19.7 %). Additionally, the superior stability of Co_2N/CoP@PNCNTs can be verified by just 3 mV shift in LSV curves after 3000 cycles. The CV curves and morphology were also checked to prove the stability of Co_2N/CoP@PNCNTs (**Figure 3i and Figure S13a-b**, Supporting Information). Meanwhile, the ESEM and corresponding EDS mapping images of Co_2N/CoP@PNCNTs after 3000 cycles of CVs were conducted to explore the morphology and element compositions in **Figure S23** (Supporting Information). The results indicate the superior stability with steady carbon nanotubes and uniform C, N, O, P, Co elements distributions. The microscopic and crystal structure of Co_2N/CoP-

@PNCNTs after 3000 cycles of CVs can be characterized by TEM and HR-TEM images in **Figure S24** (Supporting Information). It can be seen that Co_2N/CoP@PNCNTs maintains stable carbon nanotubes and the crystal structure of graphitic carbon as well as CoP remains unchanged nevertheless 3000 cycles of CVs.

What's more, linear sweep voltammetry (LSV) and cyclic voltammetry (CV) measurements of Co@C and CoP@PC were also carried out in an O_2- or N_2-saturated 0.1 M KOH solution (Figure **3a**, **3c** and **Figure S17-S18**, Supporting Information). Both Co@C and CoP@PC display an apparent oxygen reduction peak in O_2-saturated electrolyte in **Figure S17** (Supporting Information). Moreover, the electron transfer numbers of Co@C and CoP@PC per oxygen molecule for ORR determined from the RDE curves (**Figure S15**, Supporting Information) are ~3.83-3.99, which confirms a direct four-electron pathway. However, the CV reduction potential, onset potential and half-wave potential of Co@C and CoP@PC are obviously inferior to Co_2N@NCNTs and Co_2N/CoP@PNCNTs as confirmed in **Figure 3a**, **3c** and **Figure S19** (Supporting Information). Moreover, the Tafel slopes of Co@C and CoP@PC (**Figure 3f**) are respectively 120 mV dec^{-1} and 134 mV dec^{-1}, larger than that of Co_2N@NCNTs and Co_2N/CoP@PNCNTs, suggesting the slower kinetic process of ORR on the catalysts without carbon nanotubes. The chronoamperometric response after methanol addition in **Figure 3g** shows a bigger loss in Co@C and CoP@PC, indicating a worse methanol toleration performance.

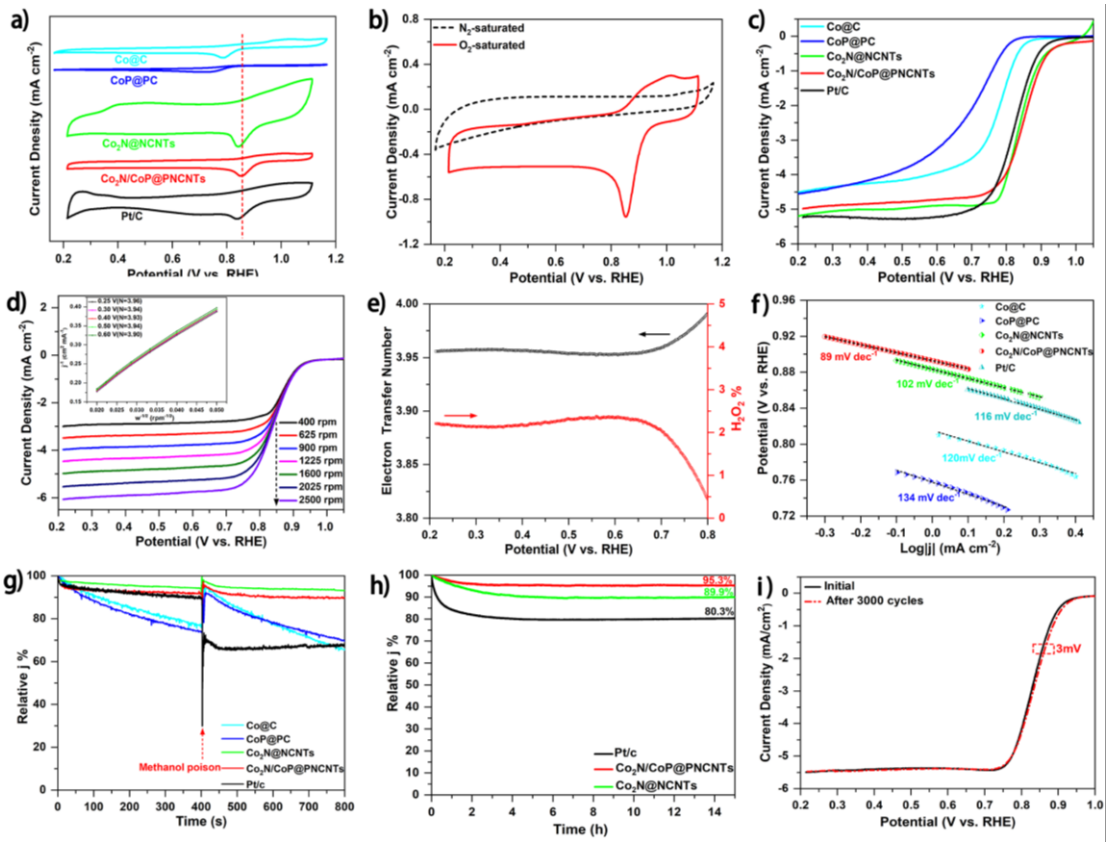

Figure 3. a) Cyclic Voltammetry (CV) curves of Co@C, CoP@PC, Co_2N@NCNTs, Co_2N/CoP@PNCNTs and Pt/C; b) CV curves of Co_2N/CoP@PNCNTs in 0.1 M N_2- and O_2-saturated KOH solution; c) Linear scan voltammetry curves of ORR with different catalysts in 0.1 M O_2-saturated KOH solution at 1600 rpm; d) Rotation-rate-dependent current-potential curves for Co_2N/CoP@PNCNTs and Koutecky-Levich plots at different potentials; e) Peroxide yield and transfer electron number of Co_2N/CoP@PNCNTs calculated from the RRDE results; f) Measured Tafel slopes of Co@C, CoP@PC, Co_2N@NCNTs, Co_2N/CoP@PNCNTs and Pt/C; g) Chronoamperometric response of Co@C, CoP@PC, Co_2N@NCNTs, Co_2N/CoP@PNCNTs and Pt/C in 0.1 M O_2-saturated KOH solution. The arrow indicates the introduction of 3 M methanol; h) Durability tests of Co_2N@NCNTs, Co_2N/CoP@PNCNTs and Pt/C at the potential of 0.5 V (vs. RHE) in 0.1 M O_2-saturated KOH at 1600 rpm; i) Linear scan voltammetry curves of Co_2N/CoP@PNCNTs before and

after 3000 cycles CVs.

The OER measurements were evaluated in 1.0 M O_2-saturated KOH electrolyte. The LSV curves without IR-correction and the overpotential comparison of various electrocatalysts in **Figure S20a-20b** (Supporting Information) confirm that Co_2N/CoP@PNCNTs affords an excellent overpotential of 329 mV at the benchmarked 10 mA cm^{-2}, which overmatches the standard IrO_2 (359 mV) and other successful OER nanocatalysts reported in **Table S7** (Supporting Information). Meanwhile, the smaller Tafel slope (107 mV dec^{-1}) of Co_2N/CoP@PNCNTs, as compared to the reference samples and commercial IrO_2, represents the outstanding OER kinetics (Figure S20c, Supporting Information). Furthermore, the CV curves in a non-faradic potential ranging from 1.07 V to 1.17 V at different scan rates are provided in **Figure S21** (Supporting Information). Double-layer capacitance (Cdl) correlated with the electrochemical active surface (ESCA) is further calculated to understand the electrode dynamics of the target electrocatalysts. As demonstrated in **Figure S20d** (Supporting Information), the calculated electrochemical double-layer capacity (Cdl) of Co_2N/CoP@PNCNTs is 4.16 mF cm^{-2}, higher than those reference samples. When the area of the bare disk electrode for our use is 0.19625cm^2, Cs is 0.80 mF cm^{-2} in **Figure S20d** (Supporting Information). Therefore, the calculated ESCA of Co_2N/CoP@PNCNTs is 5.20 cm^2, higher than that of Co_2N@NCNTs (3.96 cm^2). The large ECSA implies abundant active sites in Co_2N/CoP@PNCNTs, leading to excellent performances both in ORR and OER activities.

In consideration of the proper application and prospects of Co_2N/CoP@PNCNTs,

an assembled zinc-air battery was fabricated, as a schematic shown in **Figure 4a**. The air-cathode is composed of the catalyst Co_2N/CoP@PNCNTs, carbon substrate film with carbon paper, hydrophobic gas layer and Ni foams (**Figure 4b**). The open circuit potential of Co_2N/CoP@PNCNTs is obtained as 1.49 V approaching to the theoretic value of Zn-air battery (1.60 V),[33] and it is slightly higher than that of Co_2N@NCNTs (1.47 V) and Pt/C (1.43 V). Furthermore, the feasibility of ZABs is further verified by two batteries connected in series, which effectively powered a lighted "UCAS" green LED backlight as shown in **Figure 4c** and **4i**. The video clips of powering a lighted "UCAS" green LED backlight and a home-made fan model are provided in the Supporting Information. The maximum power density for Co_2N@NCNTs and Co_2N/CoP@PNCNTs is determined to be 129.4 mW/cm^2 and 151.1 mW/cm^2, which is equivalent to 1.2 times and 1.4 times of that obtained by the commercial Pt/C (108.8 mW/cm^2) (**Figure 4d**). The smaller charge/discharge voltage gap of Co_2N/CoP@PNCNTs is revealed in **Figure 4e**. Furthermore, the rate performance was conducted by discharging at different current densities from 2.5 mA cm^{-2} to 25 mA cm^{-2} (**Figure S26a**, Supporting Information). The corresponding discharge voltage plateau decreases from 1.31 V to 1.19 V. When the current density was brought to 2.5 mA cm^{-2}, the voltage recovers to 1.31 V. The specific capacity and energy density of Co_2N/CoP@PNCNTs are achieved as 823.8 mAh g^{-1} and 1050.1 Wh kg^{-1}, respectively, which are close to the theoretical value of 840 mAh g^{-1} and 1350 Wh kg^{-1}[69, 70], superior to those of Co_2N@NCNTs (812.7 mAh g^{-1}, 1005.4 Wh kg^{-1}) and Pt/C (788.8 mAh g^{-1}, 991.6 Wh kg^{-1}) in **Figure 4f** and **Figure S26b**

(Supporting Information). It is worthy of noting that the difference of charge potential between Co_2N@NCNTs and Co_2N/CoP@PNCNTs is about 56 mV at the current density of 10 mA cm^{-2}, which is smaller than the difference of overpotentials (81 mV) between Co_2N@NCNTs and Co_2N/CoP@PNCNTs in OER measurements. The variation (about 25 mV) between the overpotentials in OER and the charge potential in Zn-air batteries may lie in the concentration variation of electrolytes and oxygen we used in these two measurements. In the OER measurement, we adopted the condition of continuously saturated O_2 and in 1 M KOH solution, which is favorable for OER activities, thus enlarging the electrocatalytic performance difference between two catalysts. While in Zn-air batteries, the operation condition is in the unsaturated and natural air and 6 M KOH, meaning less oxygen and higher alkaline solution and it probably decreases the difference of charge potential between Co_2N@NCNTs and Co_2N/CoP@PNCNTs.

The rechargeability and stability were further conducted by galvanostatic discharge and charge cycling tests at 10 mA cm^{-2} with per cycle of 20 min. The Zn-air battery based on Co_2N/CoP@PNCNTs displays a substantial elongated lifetime with negligible voltage fading after a continuous test of 150 h for 450 cycles and a smaller voltage gap (0.75 V). As a comparison, the Co_2N@NCNTs and Pt/C reflect a worse cycling durability with a bigger voltage gap (0.98 V and 1.11 V, respectively). In addition, the galvanostatic charge and discharge cycling measurement in the assembled Zn-air battery with Co_2N/CoP@PNCNTs was conducted at the current density of 20 mA cm^{-2}. Remarkably, the battery with Co_2N/CoP@PNCNTs displays a

charge-discharge voltage of 1.01 V and superior stability without a noticeable increase in potential fading for 150 h (**Figure S27a-b**, Supporting Information). By comparing with other advanced studies listed in **Table S5-S8** (Supporting Information), our work Co_2N/CoP@PNCNTs exhibits the outstanding electrocatalytic properties as well as the equivalent ZABs performance in durability, power density and specific capacity.

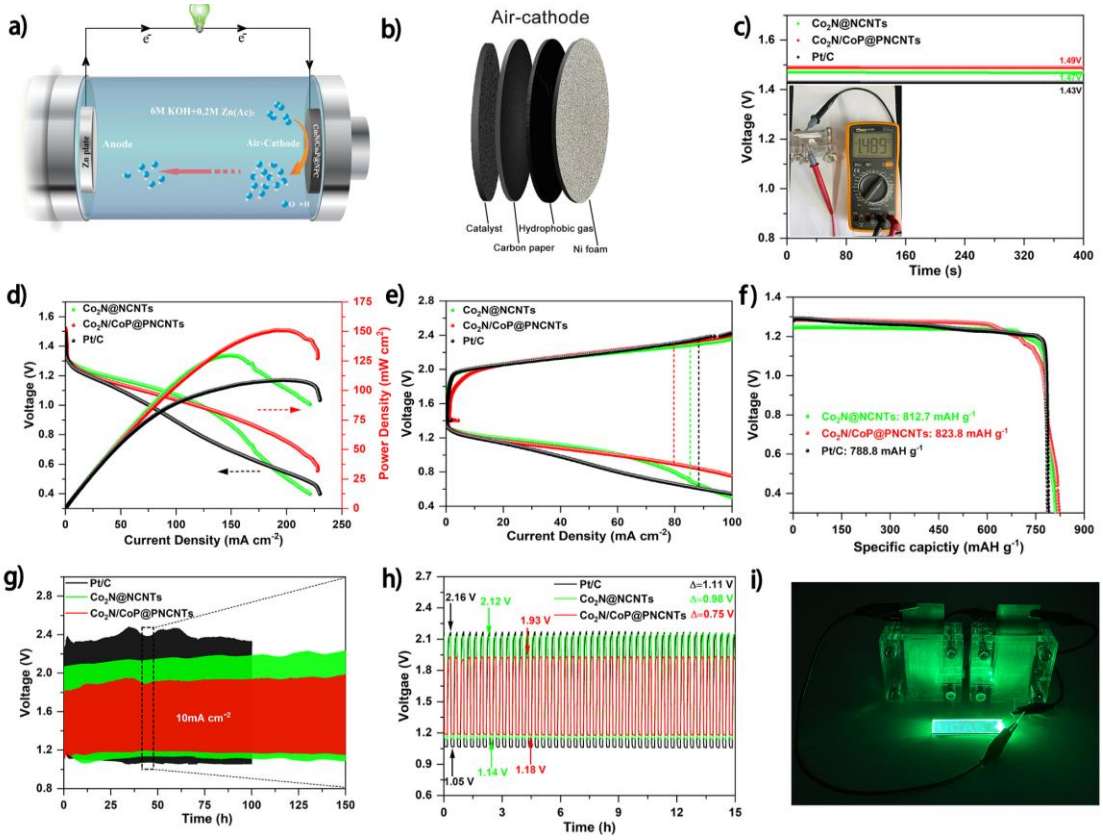

Figure 4. Zn-air battery performance with Co_2N@NCNTs, Co_2N/CoP@PNCNTs and Pt/C as the air cathode. a) Schematic illustration of the structure of Zn-air battery; b) Composition of air cathode; c) Initial open-circuit potential plots (Inset: the open circuit potential of Co_2N/CoP@PNCNTs showing the value of 1.49 V); d) Discharge polarization curves and the corresponding power density curves; e) Charge and discharge polarization curves; f) Discharge curves at the current density of 5 mA cm^{-2}; g, h) Long-term galvanostatic discharge and charge cycling stability at the current density of 10 mA cm^{-2}, where the dotted rectangular

part is enlarged in (h); i) Photograph of a lighted green LED (3.0 V) with the "UCAS" logo powered by two Zn-air batteries based on Co_2N/CoP@PNCNTs.

The excellent ORR and Zn-air batteries performances of Co_2N/CoP@PNCNTs can be credited to the synergistic effect of multicomponent and the prominent structures of Co_2N/CoP@PNCNTs which profit oxygen adsorption, desorption and reduction. Compared with Co@C, CoP@C and Co_2N@NCNTs, Co_2N/CoP@PNCNTs is endowed with N, P-doping, Co_2N and CoP simultaneously, which contributes cooperatively to ORR electrocatalytic performances. Firstly, hierarchical and mesoporous CNTs architecture supplies a large surface area (148.4 m^2 g^{-1}) with sufficient active sites and a direct and open channel which is beneficial for mass diffusion and electron transportation.[71] Moreover, N, P doping into CNTs can adjust the electronic density distributions and active the electronic states of adjacent carbon atoms, thus improving the quantity and distribution of active sites.[72-73] Furthermore, the introduction of N and P dopants can reduce the reaction barrier along the reaction path and cause the polarization of density of states at the Fermi level,[6, 74] leading to promoting adsorption and desorption of O_2. Additionally, the enriched electrons of Co_2N and CoP as the catalytically active species not only contribute to the oxygen adsorption and reduction, but also restrain carbon nanotubes shell from being corrosive and oxidized, thus guaranteeing the stability of Co_2N/CoP@PNCNTs.[75]

3. Conclusions

In summary, we have successfully developed a hierarchical core-shell nanotube conductive network by one-step carbonization-nitridation-phosphorization procedure.

It is demonstrated that the pyrolysis temperature and mass ratios of P sources have a significant impact on the morphology and the species of cobalt phosphides, thereby obtaining the optimized Co_2N@NCNTs and Co_2N/CoP@PNCNTs. The cores are composed of Co_2N or Co_2N/CoP nanoparticles protected with N, P co-doped carbon nanotubes as shell. Impressively, the obtained Co_2N/CoP@PNCNTs manifests excellent electrocatalysis activity which outperforms the commercial Pt/C for oxygen reduction reaction such as more positive CV peak potential (0.85 V), onset potential (1.07 V) and half-wave potential (0.85 V), with an excellent methanol tolerance and stability. By using the Co_2N/CoP@PNCNTs as the cost-effective air cathode in Zn-air batteries, it exhibits a high peak power density (151.1 mW cm^{-2}), an impressive specific capacity (823.8 mAh g^{-1}), and an outstanding energy density (1050.1 Wh kg^{-1}). Remarkably, the Co_2N/CoP@PNCNTs shows high cycling stabilities with 150 h at 10 mA cm^{-2}. The high catalytic performances are attributed to high surface areas exposing abundant active sites, enriched mesoporous porosity beneficial for mass transport, highly graphitized carbon support contributing to high electronical conductivity as well as the synergistic effects of highly active Co_2N and CoP hybrids. This work not only provides a promising strategy to build sophisticated phosphide-based transition metal nanostructures, but also demonstrates the great potential of cobalt phosphides and multicomponent concerted electrocatalysts in energy applications.

4. Experimental Section

4.1. Chemicals and Reagents

Pt/C (20 wt%, Johnson Matthey) and 2-aminoterephthalic acid ($C_8H_7NO_4$) were derived from Alfa Aesar. Nafion solution (5 wt%) was obtained from Sigma-Aldrich. Cobalt (II) acetate tetrahydrate ($Co(Ac)_2.4H_2O$), potassium hydroxide (KOH), zinc acetate ($Zn(Ac)_2.2H_2O$), sodium hypophosphite (NaH_2PO_2) were purchased from Sinopharm Chemical Reagent Co., Ltd with analytical reagent pure grade(A.R.) and were used without any purification. Dicyandiamide (DCDA, $C_2H_4N_4$), methanol and ethanol were provided by Aladdin. All aqueous solutions were attained from deionized water with a specific resistance of > 18.2 MΩ.cm.

4.2. Synthesis of Co-MOF

First, 2-aminoterephthalic acid (1.5 mmol) dissolved in methanol (50 mL) was added dropwise into $Co(Ac)_2.4H_2O$ (4 mmol) dispersed in methanol (100 mL) and immediately formed the pink precipitate in the solution. The solid product was centrifugally rinsed, afterwards it was dispersed with deionized water to regulate PH= 7. The above solution was immediately transferred into a Teflon-lined stainless-steel autoclave (45 mL), tightly sealed and kept in an oven at 160 °C for 12 h. After naturally cooling down to room temperature, the pink precipitate was washed and centrifuged successively with deionized water and methanol solution. The final product, entitled as Co-MOF, was dried at 80 °C for 8 h in a vacuum oven for further use.

4.3. Synthesis of Co_2N@NCNTs and Co_2N/CoP@PNCNTs

The as-prepared Co-MOF product (50 mg) and dicyandiamide (DCDA, 1 g) were placed in two separated ceramic boats with the as-prepared Co-MOF at the

downstream side of the Ar flow (60 sccm). With a heating ramp of 10 °C min^{-1}, the temperature was first increased to 400 °C and kept for 2 h. Then the temperature was further raised to 800 °C with the same rate and maintained for another 4h. The black product was collected and marked as Co_2N@NCNTs.

The as-prepared Co-MOF product (50 mg) and sodium hypophosphite (NaH_2PO_2, 0.5 g) were placed in the same ceramic boat. Dicyandiamide (1 g) was put in the other ceramic boat. With the sequence, DCDA was at the upstream, then NaH_2PO_2 at the midstream and as-prepared Co-MOF product at the downstream side at the Ar flow (60 sccm). The product was first heated at 400 °C for 2 h at a heating ramp of 10 °C min^{-1}, then raised to 800 °C with the same rate and maintained at this temperature for another 4 h. The black product was collected and recorded as Co_2N/CoP@PNCNTs.

The other temperatures and mass ratios of Co_2N@NCNTs and Co_2N/Co_xP@PN-CNTs were described in **Experiment Section 1.1-1.3** (Supporting Information). Furthermore, the synthetical details of Co@C and CoP@PC are also described in **Experiment Section 1.4-1.5** (Supporting Information).

4.4. Characterization of Materials

The crystal structures of the obtained materials were performed on X-ray diffraction (XRD) measurements (PANalytical B.V. X'Pert3 Powder) with a Cu–K(alpha) source at 40 kV with 40 mA. The morphology and elemental mapping analysis of solid samples were characterized on a field-emission environmental scanning electron microscope (ESEM, FEI Quattro S) equipped with an energy dispersive X-ray analysis (EDX, Ametek Element E1868-C2B) spectroscopy. The

transmission electron microscopic (TEM) images were carried out on a FEI Tecnai G2 F30 transmission electron microscopy at an accelerating voltage of 300 kV. X-ray photoelectron spectroscopic (XPS) measurements were conducted on an ESCALAB 250Xi instrument (Thermo Fisher Scientific). Raman scattering spectra were measured to receive the degree of graphitization on a Renishaw inVia Reflex Raman Microscope System with an excitation wavelength of 532 nm. Infrared spectroscopy spectra were performed to measure types of chemical bonds on Perkinelmer Spectrum Two, USA. N_2 adsorption/desorption isotherms were acquired at liquid nitrogen temperature (77 K) using an ASAP-2020 physisorption analyzer (Micromeritics) after dehydration under vacuum at 220 °C for 9 h. The total surface areas were calculated by using the Brunauer-Emmett-Teller method and the volume of pores were calculated by using the single point model.

4.5. Electrocatalysis and Electrochemical Measurements

The electrochemical and electrocatalysis measurements linked with ORR were conducted with a CHI 760E electrochemical workstation using a standard three-electrode cell. A rotating disk electrode (RDE) and a rotating ring disk electrode (RRDE) were functioned to measure the activity and stability of the samples on a Pine Research Instrumentation (AF01WV10). A Platinum wire and a saturated calomel electrode were treated as the counter and reference electrode, respectively. A glassy carbon rotating disk (5 mm in diameter) or a rotating ring-disk electrode with a Pt ring, coating the catalyst inks was employed as the working electrode. 2.5 mg of the catalyst was ultrasonically dispersed in 1 mL of absolute ethanol for 1 h and then 30

μL of 5 wt% Nafion solution was added and ultrasonically dispersed for 0.5 h to form homogeneous inks. The inks were decorated on a freshly polished GC disk by drop-casting with a loading mass of 0.2 mg cm^{-2}. For comparison, a commercial Pt/C (20 wt% Johnson Matthey) catalyst was fabricated in the same way. All potentials measured against a SCE electrode in this work were converted to potential versus RHE with the Nernst equation $E_{RHE} = E_{SCE} + 0.0592\ pH + 0.244\ V$.

The cyclic voltammetry was made to investigate the ORR performance in N_2/O_2-saturated 0.1 M KOH solution at a sweep rate of 10 mV s^{-1}. RDE measurements were carried out by linear sweep voltammetry curves under O_2-saturated 0.1 M KOH from 0 to -0.8 V at 5 mV s^{-1} with various rotating speeds from 400 to 2500 rpm. RRDE measurements were investigated using a CHI 760E electrochemical workstation equipped at 1600 rpm. Furthermore, the Tafel slopes were acquired to assess the kinetics of the catalysts by plotting the curves of E_{RHE} versus Log|J|.

The transferred electron numbers (n) were calculated from the K–L equations (1)-(2). In addition, the electron transfer numbers (n) and the yield of hydrogen peroxide ($\%H_2O_2$) released during ORR process were calculated based on the following equations (3)-(4).

$$\frac{1}{J} = \frac{1}{J_L} + \frac{1}{J_K} = \frac{1}{Bw^{\frac{1}{2}}} + \frac{1}{J_K} \quad (1)$$

$$B = 0.62nFC_0(D_0)^{2/3} \nu^{1/6} \quad (2)$$

Where J, J_K and J_L represent the measured current density, kinetic, and diffusion limiting current densities, respectively. w is the electrode rotation speed, F is the

Faraday constant (96485 C mol^{-1}), D_0 is the diffusion coefficient of O_2 (1.9×10^{-5} cm^2 s^{-1}), *v* is the kinetic viscosity the electrolyte (0.01 cm^2 s^{-1}), and C_0 is the concentration of O_2 (1.2×10^{-6} mol cm^{-3}), n is the overall number of electrons gained per O_2.

$$n = 4 \times \frac{I_D}{\frac{I_R}{N} + I_D} \quad (3)$$

$$\%H_2O_2 = 200 \times \frac{I_R/N}{\frac{I_R}{N} + I_D} \quad (4)$$

where I_D is the disk current, I_R is the ring current, and N is the collection coefficient of the Pt ring (N=0.37).

On the one hand, the durability of the catalyst for ORR was evaluated by the chronoamperometry analysis at 0.5 V *vs* RHE in O_2-saturated 0.1 M KOH solution. On the other hand, the accelerated durability of the catalysts was implemented through recording linear sweep voltammetry (LSV) curves of ORR at the 1st and 3000th cycles of CV measurements in O_2-saturated 0.1 M KOH solution with the rotating rate at 1600 rpm. Furthermore, the methanol tolerance test was assessed by the current-time (I-T) chronoamperometric response before and after the addition of methanol at 400 s.

What's more, the OER measurements were conducted in a standard three-electrode by a CHI 760E workstation. Linear sweep voltammetry (LSV) was performed by the rotating disk electrode technique at 5 mV s^{-1}. The overpotential of OER(η) can be calculated by the equation (5):

$$\eta = E_{RHE} - 1.23\ V \quad (5)$$

Where E_{RHE} represents the potential versus reversible hydrogen electrode.

The Tafel slope is calculated according to the equation (6). Furthermore, the ECSA was determined based on the double-layer capacitance (Cdl) by measuring the CV curves of the electrode at a non-Faradic region of 1.27 V to 1.37 V with different scan rates of 20, 40, 60, 80, and 100 mV s^{-1}. The ESCA of the catalysts can be calculated according to the equation (7).

$$\eta = a + b \log(j) \quad (6)$$

$$ESCA = Cdl / Cs \quad (7)$$

Where η is the overpotential, a is a constant, b is the Tafel slope, and j is the current density. Cdl is the electrochemical double-layer capacitance of various electrocatalysts and Cs is the double-layer capacitance of bare disk electrode.

4.6. Tests of Electrocatalysts as Air-Cathode Electrodes in ZABs

The liquid Zn-air battery was customized with both anode and cathode areas of 2 cm^2 and combined with the polished Zinc plate as the anode, while with the prepared Co_2N@NCNTs, Co_2N/CoP@PNCNTs catalyst and commercial Pt/C (20 wt.%) coated on carbon paper (1 mg cm^{-2}) coupled with a hydrophobic gas layer as the air cathodes. Afterwards, the electrolyte containing 6 M KOH with 0.2 M Zn $(Ac)_2$ was added dropwise into the assembled Zn-air battery. The battery was stewing for one night to make the electrolyte thoroughly wet the anode and cathode for a stable state. The charge and discharge polarization curves were collected on an electrochemical workstation (CHI 760E) with the open circuit potential (1.49 V for Co_2N/CoP@PNCNTs and 1.43 V for commercial Pt/C) as the initial potential at the scan rate of 5 mV s^{-1}. The chronopotentiometry was performed on LAND-CT2001A

at a current density of 5 mA cm^{-2} to evaluate the specific capacity, energy density and at various current densities in the range from 2.5 to 25 mA cm^{-2}. The cycling performance of rechargeable Zn-air batteries was also conducted on LAND-CT2001A at a current density of 10 mA cm^{-2} with periods of 10 min per cycle. Following the corresponding specific capacity (mAh g^{-1}) and energy density (Wh kg^{-1}), we can calculate using the following equations (8)-(9):

$$Q = \frac{I*T}{m} \quad (8)$$

$$E_D = Q*E \quad (9)$$

Where Q and E_D stand for specific capacity (mAh g^{-1}) and energy density (Wh kg^{-1}), I and T represent the current (A) and service hours (h), m is the weight of consumed Zn (g), and E is discharge voltage (V).

Supporting Information

Supporting information is available from the author.

Acknowledgements

The authors acknowledge the financial support from the National Key Research and Development Program of China (2017YFA0207204 and 2016YFA0203101), the National Natural Science Foundation of China (21836002 and 21876190), and the Fundamental Research Funds for the Central Universities (2020001840).

Conflict of Interest

The authors declare no conflict of interest.

Data Availability

The raw/processed data required to reproduce these findings cannot be shared at this time as the data also form part of an ongoing study.

References

[1] M. K. Debe, *Nature* **2012,** *486* (7401), 43-51.

[2] L. An, Z. Y. Zhang, J. R. Feng, F. Lv, Y. X. Li, R. Wang, M. Lu, R. B. Gupta, P. X. Xi, S. Zhang, *J. Am. Chem. Soc.* **2018,** *140* (50), 17624-17631.

[3] J. Yin, Y. X. Li, F. Lv, M. Lu, K. Sun, W. Wang, L. Wang, F. Y. Cheng, Y. F. Li, P. X. Xi, S. J. Guo, *Adv. Mater.* **2017,** *29* (47), 1704681.

[4] J. Yin, Y. X. Li, F. Lv, Q. H. Fan, Y. Q. Zhao, Q. L. Zhang, W. Wang, F. Y. Cheng, P. X. Xi, S. J. Guo, *ACS Nano* **2017,** *11* (2), 2275-2283.

[5] X. H. Gao, H. X. Zhang, Q. G. Li, X. G. Yu, Z. L. Hong, X. W. Zhang, C. D. Liang, Z. Lin, *Angew. Chem., Int. Ed.* **2016,** *55* (21), 6290-4.

[6] T. P. Zhou, N. Zhang, C. Z. Wu, Y. Xie, *Energy Environ. Sci.* **2020,** *13* (4), 1132-1153.

[7] X. W. Lv, W. S. Xu, W. W. Tian, H. Y. Wang, Z. Y. Yuan, *Small* **2021,** *17* (38), e2101856.

[8] J. Li, X. Gao, L. Zhu, M. N. Ghazzal, J. Zhang, C. H. Tung, L. Z. Wu, *Energy Environ. Sci.* **2020,** *13* (5), 1326-1346.

[9] Y. Niu, M. L. Xiao, J. B. Zhu, T. T. Zeng, J. D. Li, W. Y. Zhang, D. Su, A. P. Yu, Z. W. Chen, *J. Mater. Chem. A* **2020,** *8* (18), 9177-9184.

[10] C. F. Xia, Y. S. Zhou, C. H. He, A. I. Douka, W. Guo, K. Qi, B. Y. Xia, *Small Sci.* **2021**,2100010.

[11] Y. Jiang, Y. P. Deng, J. Fu, D. U. Lee, R. L. Liang, Z. P. Cano, Y. S. Liu, Z. Y. Bai, S. Hwang, L. Yang, D. Su, W. G. Chu, Z. W. Chen, *Adv. Energy Mater.* **2018,** *8* (15), 1702900.

[12] Y. B. Li, C. Zhong, J. Liu, X. Q. Zeng, S. X. Qu, X. P. Han, Y. D. Deng, W. B. Hu, J. Lu, *Adv. Mater.* **2018,** *30* (4), 1703657.

[13] Z. P. Miao, Y. Xia, J. S. Liang, L. F. Xie, S. Q. Chen, S. Z. Li, H. L. Wang, S. Hu, J. T. Han, Q. Li, *Small* **2021,** *17* (29), e2100735.

[14] Z. T. Li, L. Q. Wei, W. J. Jiang, Z. P. Hu, H. Luo, W. N. Zhao, T. Xu, W. T. Wu, M. B. Wu, J. S. Hu, *Appl. Catal., B* **2019,** *251*, 240-246.

[15] Q. Yang, Y. Jia, F. F. Wei, L. Z. Zhuang, D. J. Yang, J. Z. Liu, X. Wang, S. Lin, P. Yuan, X. D. Yao, *Angew. Chem., Int. Ed.* **2020,** *59* (15), 6122-6127.

[16] H. C. Yang, Y. J. Zhang, F. Hu, Q. B. Wang, *Nano Lett.* **2015,** *15* (11), 7616-20.

[17] P. Tan, B. Chen, H. R. Xu, W. Z. Cai, W. He, M. Ni, *Appl. Catal., B* **2019,** *241*, 104-112.

[18] I. S. Amiinu, X. B. Liu, Z. H. Pu, W. Q. Li, Q. D. Li, J. Zhang, H. L. Tang, H. N. Zhang, S. C. Mu, *Adv. Fun. Mater.* **2018,** *28* (5), 1704638.

[19] W. J. Liu, X. Hu, H. C. Li, H. Q. Yu, *Small* **2018,** *14* (34), e1801878.

[20] G. Y. Zhou, M. Li, Y. L. Li, H. Dong, D. M. Sun, X. E. Liu, L. Xu, Z. Q. Tian, Y. W. Tang, *Adv. Funct. Mater.* **2019,** *30* (7), 1905252.

[21] H. Li, X. L. Zhao, H. L. Liu, S. Chen, X. F. Yang, C. X. Lv, H. W. Zhang, X. L. She, D. J. Yang, *Small* **2018,** *14* (41), e1802824.

[22] D. X. Liu, B. Wang, H. G. Li, S. F. Huang, M. M. Liu, J. Wang, Q. J. Wang, J. J. Zhang, Y. F.

Zhao, *Nano Energy* **2019,** *58*, 277-283.
[23] E. O. Eren, N. Özkan, Y. Devrim, *Int. J. Hydrogen Energy* **2020,** *45* (58), 33957-33967.
[24] S. S. A. Shah, T. Najam, M. S. Javed, M. M. Rahman, P. Tsiakaras, *ACS Appl. Mater. Interfaces* **2021,** *13* (19), 23191-23200.
[25] S. Yuan, L. L. Cui, Z. Y. Dou, X. Ge, X. Q. He, W. Zhang, T. Asefa, *Small* **2020,** *16* (40), e2000742.
[26] L. Du, L. L. Luo, Z. X. Feng, M. Engglhard, X. H. Xie, B. H. Han, J. M. Sun, J. H. Zhang, G. P. Yin, C. M. Wang, Y. Wang, Y. Y. Shao, *Nano Energy* **2017,** *39*, 245-252.
[27] K. N. Dinh, Q. H. Liang, C. F. Du, J. Zhao, A. I. Y. Tok, H. Mao, Q. Y. Yan, *Nano Today* **2019,** *25*, 99-121.
[28] H. Li, Q. Li, P. Wen, Williams, T. B., Adhikari, S., C. C. Dun, C. Lu, D. Itanze, L. Jiang, D. L. Carroll, G. L. Donati, P. M. Lundin, Y. J. Qiu, S. M. Geyer, *Adv. Mater.* **2018,** *30* (9), 1705796.
[29] Y. L. Dang, J. K. He, T. L. Wu, L. P. Yu, P. Kerns, L. Y. Wen, J. Ouyang, S. L. Suib, *ACS Appl. Mater. Interfaces* **2019,** *11* (33), 29879-29887.
[30] X. M. Hu, S. L. Zhang, J. W. Sun, L. Yu, X. Y. Qian, R. D. Hu, Y. N. Wang, H. G. Zhao, J. W. Zhu, *Nano Energy* **2019,** *56*, 109-117.
[31] H. Li, Q. Li, P. Wen, T. B. Williams, S. Adhikari, C. Dun, C. Lu, D. Itanze, L. Jiang, D. L. Carroll, G. L. Donati, P. M. Lundin, Y. Qiu, S. M. Geyer, *Adv. Mater.* **2018**, 30, 1705796.
[32] Y. Yan, Y. Y. Xu, B. Zhao, Y. Xu, Y. Gao, G. D. Chen, W. B. Wang, B. Y. Xia, *J. Mater. Chem. A* **2020,** *8*, 5070-5077.
[33] X. W. Lv, J. T. Ren, Y. S. Wang, Y. P. Liu, Z. Y. Yuan, *ACS Sustainable Chem. Eng.* **2019,** *7* (9), 8993-9001.
[34] Y. Li, Z. H. Dong, L. F. Jiao, *Adv. Energy Mater.* **2019,** *10* (11), 1902104.
[35] H. T. Liu, J. Y. Guan, S. X. Yang, Y. H. Yu, R. Shao, Z. P. Zhang, M. L. Dou, F. Wang, Q. Xu, *Adv. Mater.* **2020,** *32* (36), e2003649.
[36] Q. Shi, Q. Liu, Y. P. Zheng, Y. Q. Dong, L. Wang, H. T. Liu, W. Y. Yang, *Energy Environ. Mater.* **2021,** 0, 1-9.
[37] G. C. Philip, S. A. Michael, A. Phaedon, *Science* **2001,** 1058782.
[38] G. W. Zhang, B. Wang, J. L. Bi, D. Q. Fang, S. C. Yang, *J. Mater. Chem. A* **2019,** *7* (10), 5769-5778.
[39] L. L. Zou, C. C. Hou, Z. Liu, H. Pang, Q. Xu, *J. Am. Chem. Soc.* **2018,** *140* (45), 15393-15401.
[40] D. N. Futaba, K. Hata, T. Yamada, T. Hiraoka, Y. Hayamizu, Y. Kakudate, O. Tanaike, H. Hatori, M. Yumura, S. Iijima, *Nat. Mater.* **2006,** *5* (12), 987-94.
[41] M. Y. Tan, Y. Y. Xiao, W. H. Xi, X. F. Lin, B. F. Gao, Y. L. Chen, Y. Zheng, B. Z. Lin, *Journal of Power Sources* **2021,** *490*.
[42] F. Z. Song, W. Li, J. Q. Yang, G. Q. Han, T. Yan, X. Liu, Y. Rao, P. L. Liao, Z. Cao, Y. J. Sun, *ACS Energy Lett.* **2019,** *4* (7), 1594-1601.
[43] X. L. Ge, Z. Q. Li, L. W. Yin, *Nano Energy* **2017,** *32*, 117-124.
[44] R. Zhang, C. Tang, R. M. Kong, G. Du, Asiri, A. M., L. Chen, X. P. Sun, *Nanoscale* **2017,** *9* (14), 4793-4800.
[45] T. Chen, J. Ma, S. Y. Chen, Y. M. Wei, C. S. Deng, J. C. Chen, J. Q. Hu, W. P. Ding, *Chem. Eng. J.* **2021,** *415*.
[46] X. L. Wu, G. S. Han, H. Wen, Y. Y. Liu, L. Han, X. Y. Cui, J. J. Kou, B. J. Li, J. C. Jiang, *Energy Environ. Mater.* **2021,** 0, 1-9.

[47] J. G. Zheng, A. N. Xu, A. J. Wu, X. D. Li, *ACS Appl. Mater. Interfaces* **2021,** *13* (18), 21231-21240.

[48] Y. Pan, K. A. Sun, S. J. Liu, X. Cao, K. L. Wu, W. C. Cheong, Z. Chen, Y. Wang, Y. Li, Y. Q. Liu, D. S. Wang, Q. Peng, C. Chen, Y. D. Li, *J. Am. Chem. Soc.* **2018,** *140* (7), 2610-2618.

[49] Q. Ke, L. Yang, Y. B. Gao, X. L. Wu, F. Chen, S. J. Liu, H. J. Lin, C. Z. Yuan, J. R. Chen, *Nanotechnology* **2020,** *31* (16), 165401.

[50] E. J. Popczun, C. G. Read, C. W. Roske, N. S. Lewis, R. E. Schaak, *Angew. Chem., Int. Ed.* **2014,** *53* (21), 5427-30.

[51] D. Yoon, D. H. Kim, K. Y. Chung, W. Y. Chang, S. M. Kim, J. Kim, *Carbon* **2016,** *98*, 213-220.

[52] J. H. Zhang, Q. H. Kong, D. Y. Wang, *J. Mater. Chem. A* **2018,** *6* (15), 6376-6386.

[53] Y. Zhang, Q. Sun, K. S. Xia, B. Han, C. G. Zhou, Q. Gao, H. Q. Wang, S. Pu, J. P. Wu, *ACS Sustainable Chem. Eng.* **2019,** *7* (6), 5717-5726.

[54] M. R. Gao, X. Cao, Q. Gao, Y. F. Xu, Y. R. Zheng, J. Jiang, S. H. Yu, *ACS Nano* **2014,** 84, 3970-3978 .

[55] J. Bai, B. J. Xi, H. Z. Mao, Y. Lin, X. J. Ma, J. K. Feng, S. Xiong, *Adv. Mater.* **2018,** *30* (35), e1802310.

[56] Y. Zheng, Y. Jiao, L. H. Li, T. Xing, Y. Chen, Jaroniec Mietek, S. Z. Qiao, *ACS Nano* **2014,** 85, 5290-5296.

[57] Y. Y. Guo, P. F. Yuan, J. N. Zhang, H. C. Xia, F. Y. Cheng, M. F. Zhou, J. Li, Y. Y. Qiao, S. C. Mu, Q. Xu, *Adv. Func. Mater.* **2018,** *28* (51), 1805641.

[58] Z. Z. Zhu, Q. Q. Xu, Z. T. Ni, K. F. Luo, Y. Y. Liu, D. S.Yuan, *ACS Sustainable Chem. Eng.* **2021,** *9* (40), 13491-13500.

[59] T. Ikeda, M. Boero, S. F. Huang, K. Terakura, M. Oshima, J. Ozak, *J. Phys. Chem. C* **2008**, *112*, 14706.

[60] H. W. Liang, X. D. Zhuang, S. Brüller, X. L. Feng, K. Müllen, *Nat.Commun.* **2014**, *5*, 4973.

[61] D. R. Liyanage, S. J. Danforth, Y. Liu, M. E. Bussell, S. L. Brock, *Chem. Mater.* **2015,** *27* (12), 4349-4357.

[62] R. Jin, X. Li, Y. Sun, H. Shan, L. Fan, D. Li, X. Sun, *ACS Appl. Mater. Interfaces* **2018**, *10*, 14641.

[63] Q. Liu, J. Tian, W. Cui, P. Jiang, N. Cheng, A.M. Asiri, X. Sun, *Angew. Chem. Int. Ed.* **2014**, *53*, 6710-6714.

[64] L. Hu, F. Wang, M. S. Balogun, Y. Tong, *J. Mater. Sci. Technol.* **2020**, *55*, 203.

[65] S. Chen, Y. Zheng, B. Zhang, Y. Y. Feng, J. X. Zhu, J. S. Xu, C. Zhang, W. Feng, T. X. Liu, *ACS Appl. Mater. Interfaces* **2019,** *11* (1), 1384-1393.

[66] D. Deng, L. Yu, X. Chen, G. Wang, L. Jin, X. Pan, J. Deng, G. Sun, X. Bao, *J. Mater. Chem. A* **2013**, *1*, 14868.

[67] Z. Y. Wang, Y. F. Dong, H. J. Li, Z. B. Zhao, H. B. Wu, C. Hao, S. H. Liu, J. S. Qiu, X. W. Lou, *Nat. Commun.* **2014,** *5*, 5002.

[68] Q. N. Liu, Z. Hu, Y. R. Liang, L. Li, C. Zou, H. L. Jin, S. Wang, H. M. Lu, Q. F. Gu, S. L. Chou, Y. Liu, S. X. Dou, *Angew. Chem., Int. Ed.* **2020,** *59* (13), 5159-5164.

[69] K. Wang, J. P. Liu, Z. H. Tang, L. G. Li, Z. Wang, M. Zubair, F. Ciucci, L. Thomsen, J. Wright, N. M. Bedford, *J. Mater. Chem. A* **2021,** *9* (22), 13044-13055.

[70] D. Wang, P. X. Yang, H. Xu, J. Y. Ma, L. Du, G. X. Zhang, R. P. Li, Z. Jiang, Y. Li, J. Q. Zhang, M. Z. An, *J. Power Sources* **2021,** *485*.

[71] J. C. Gao, J. M. Wang, L. J. Zhou, X. Y. Cai, D. Zhan, M. Z. Hou, L. F. Lai, *ACS Appl. Mater. Interfaces* **2019,** 11 (10), 10364-10372.
[72] F. Wan, L. L. Zhang, X. Dai, X. Y. Wang, Z. Q. Niu, J. Chen, *Nat. Commun.* **2018,** *9* (1), 1656.
[73] F. Y. Cheng, J. Chen, *Chem. Soc. Rev.* **2012,** *41* (6), 2172-92.
[74] H. Cheng, K. Xu, L. L. Xing, S. Liu, Y. Gong, L. Gu, L. D. Zhang, C. Z. Wu, *J. Mater. Chem. A* **2016,** *4* (30), 11775-11781.
[75] S. H. Ahn, A. Manthiram, *Small* **2017,** *13* (40), 1702068.

Table of Contents

Graphics

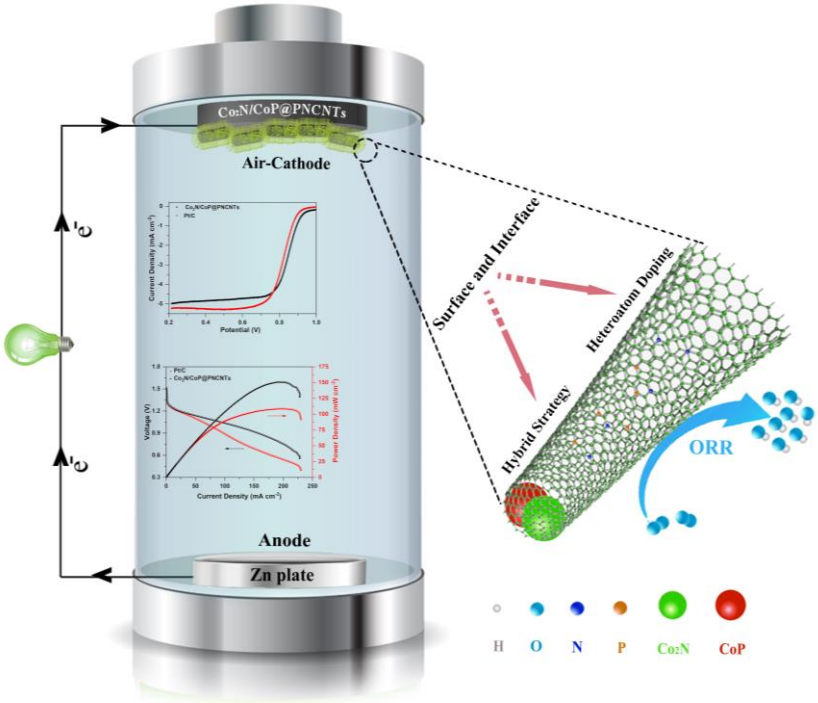

Description:

Inspired by surface and interface nanoengineering strategy, Core-shell Co_2N/CoP@PNCNTs has been designed to present superior ORR and Zn-air batteries performances, owing to the synergistic effect of Co_2N/CoP as the core and N, P doped carbon nanotubes as the shell, with large specific surface area, excellent electricity conductivity, enriched electronic structure contributing to lower energy barrier and stable shell protection.